An activatable PET imaging radioprobe is a dynamic reporter of myeloperoxidase activity in vivo

Cuihua Wang[a,1], Edmund Keliher[a,1], Matthias W. G. Zeller[a], Gregory R. Wojtkiewicz[a], Aaron D. Aguirre[a,b], Leonard Buckbinder[c], Hye-Yeong Kim[a], Jianqing Chen[c], Kevin Maresca[c], Maaz S. Ahmed[a], Negin Jalali Motlagh[a], Matthias Nahrendorf[a], and John W. Chen[a,d,2]

[a]Center for Systems Biology, Massachusetts General Hospital and Harvard Medical School, Boston, MA 02114; [b]Cardiology Division, Massachusetts General Hospital and Harvard Medical School, Boston, MA 02114; [c]Pfizer World Wide Research and Development, Cambridge, MA 02139; and [d]Institute for Innovation in Imaging, Department of Radiology, Massachusetts General Hospital, Boston, MA 02114

Edited by Michael E. Phelps, University of California, Los Angeles, CA, and approved May 2, 2019 (received for review October 26, 2018)

Myeloperoxidase (MPO) is a critical proinflammatory enzyme implicated in cardiovascular, neurological, and rheumatological diseases. Emerging therapies targeting inflammation have raised interest in tracking MPO activity in patients. We describe ^{18}F-MAPP, an activatable MPO activity radioprobe for positron emission tomography (PET) imaging. The activated radioprobe binds to proteins and accumulates at sites of MPO activity. The radioprobe ^{18}F-MAPP has a short blood half-life, remains stable in plasma, does not demonstrate cytotoxicity, and crosses the intact blood–brain barrier. The ^{18}F-MAPP imaging detected sites of elevated MPO activity in living mice embedded with human MPO and in mice induced with chemical inflammation or myocardial infarction. The ^{18}F-MAPP PET imaging noninvasively differentiated varying amounts of MPO activity, competitive inhibition, and MPO deficiency in living animals, confirming specificity and showing that the radioprobe can quantify changes in in vivo MPO activity. The radiosynthesis has been optimized and automated, an important step in translation. These data indicate that ^{18}F-MAPP is a promising translational candidate to noninvasively monitor MPO activity and inflammation in patients.

PET imaging | myeloperoxidase | inflammation

Inflammation plays a key role in highly prevalent diseases, including many cardiovascular (1, 2), neurological (3), and rheumatological diseases (4). While an appropriate immune response can be beneficial and effect repair, aberrant activation of this response recruits excessive proinflammatory cells to cause damage. Genome-wide association studies of Alzheimer's disease (5) and myocardial infarction (6) showed that genes encoding inflammation-related factors can change the risk of developing these diseases. Although blood level of C-reactive protein has been used successfully to develop canakinumab in the Canakinumab Anti-Inflammatory Thrombosis Outcomes Study trial, blood biomarkers are indirect assessments and cannot identify the locations of inflammation and could be limited by inflammation elsewhere from off-target diseases and conditions. As such, inflammatory blood biomarkers are best used in large phase 3 trials where noise from individual patients is averaged out. For early phase drug development as well as for personalized therapy, more precise reporters of damaging inflammation are needed. Thus, there has been growing interest to identify imaging biomarkers for damaging inflammation to study its role in human diseases, identify patients at risk, and guide the development of anti-inflammatory therapies (7, 8).

Myeloperoxidase (MPO) is one such potential biomarker. Through transcriptomic profiling in a heart transplant model MPO has been identified to be highly expressed by proinflammatory cells but not by reparative cells (9). Abundant in proinflammatory innate immune cells, including neutrophils, monocytes, macrophages, and microglia, MPO catalyzes the formation of hypochlorous acid and other reactive oxygen and nitrogen species (10). MPO and its products not only kill pathogens in host defense but also oxidize lipids, proteins, DNA, and RNA to cause protein aggregation, cell signaling interruption, mutagenesis, and tissue damage (11). MPO and its excessive production of oxidants are implicated in a variety of acute and chronic diseases, including atherosclerosis (12), atrial fibrillation (13), myocardial infarction (14, 15), Alzheimer's disease (16), multiple sclerosis (17, 18), Parkinson's disease (19), and vasculitis (20). To combat MPO's deleterious effects, MPO inhibitors are being developed and tested in animal and human studies, which include PF-2999 for cardiovascular diseases (21), AZD3241 for Parkinson's disease (22), and PF-1355 for vasculitis and glomerulonephritis (23), among others.

Among the current imaging methods to detect MPO activity and its reactive species, bioluminescent luminol (24, 25), L-012 (26), fluorescent oxazine conjugated nanoparticles (27), sulfonaphthoaminophenyl fluorescein (28) and bis-5-HT-DTPA-Gd (MPO-Gd) (29) for magnetic resonance imaging (MRI) have been developed for in vivo imaging applications. However, most of the bioluminescence- and fluorescence-based agents target one or several reactive oxygen species or reactive nitrogen species and are not specific to MPO (30). These agents also have shallow depth of penetration, which limits their translational potential for human use. MPO-Gd is limited by the relatively lower detection sensitivity

Significance

The innate immune response mediates tissue damage in many diseases, but available clinical imaging technologies do not distinguish between damaging and beneficial immune responses. We developed and validated a positron emission tomography radioprobe to noninvasively report on the activity of the damaging enzyme myeloperoxidase secreted by proinflammatory innate immune cells. The high sensitivity and specificity of the radioprobe enable the detection of damaging inflammation at an earlier stage than currently possible. Such early detection could lead to early treatment before irreversible damage occurs. With its properties characterized and synthesis automated, this radioprobe is a promising imaging biomarker ready for translation to track many diseases, including cardiovascular, neurological, and rheumatological diseases.

Author contributions: C.W., E.K., L.B., M.N., and J.W.C. designed research; C.W., E.K., M.W.G.Z., G.R.W., A.D.A., H.-Y.K., M.S.A., N.J.M., and J.W.C. performed research; C.W., E.K., A.D.A., L.B., H.-Y.K., J.C., K.M., M.S.A., and J.W.C. contributed new reagents/analytic tools; C.W., E.K., M.W.G.Z., G.R.W., A.D.A., H.-Y.K., N.J.M., M.N., and J.W.C. analyzed data; and C.W., E.K., and J.W.C. wrote the paper.

Conflict of interest statement: This study was partly funded by a research grant from Pfizer. L.B., J.C., and K.M. are employees of Pfizer. However, Pfizer did not influence the analysis or interpretation of the data. C.W., E.K., and J.W.C. have filed a patent application on the imaging technology described in the article.

This article is a PNAS Direct Submission.

[1]C.W. and E.K. contributed equally to this work.

[2]To whom correspondence may be addressed. Email: jwchen@mgh.harvard.edu.

This article contains supporting information online at www.pnas.org/lookup/suppl/doi:10.1073/pnas.1818434116/-/DCSupplemental.

Published online May 23, 2019.

intrinsic to MRI. Single-photon emission computed tomography (SPECT) analogs of MPO-Gd formed by substituting Gd with ^{111}In (31, 32) or ^{67}Ga (33) have greater detection sensitivity but have a long radioactive half-life of ∼3 d and, like MPO-Gd, cannot cross the blood–brain barrier. These issues have hampered the translation and application of these agents to benefit patients. To overcome these limitations and enable rapid translation, we developed, characterized, and validated an ^{18}F-based positron emission tomography (PET) imaging radioprobe, without the need for a metal center or chelating backbone, to be a translational candidate to noninvasively report MPO activity and damaging inflammation in vivo.

Results

Synthesis of Nonradioactive Compound ^{19}F-MAPP. The nonradioactive compound ^{19}F-MAPP (myeloperoxidase-activatable PET probe) was synthesized according to Fig. 1*A*. Intermediate 1, which was obtained from *N*′,*N*′-dicyclohexylcarbodiimide (DCC) coupling of 5-hydroxytryptophan and 5-hydroxyindole acetic acid, underwent coupling reaction with intermediate 2 (*SI Appendix*, Scheme S1) using *N*-(3-dimethylaminopropyl)-*N*′-ethylcarbodiimide (EDC) hydrochloride and hydroxybenzotriazole (HOBt) to give compound 3. Direct fluorination of compound 3, however, did not result in the desired compound since it decomposed under fluorinating conditions. After screening for different protective groups, we found *tert*-butyloxycarbonyl (Boc) to be suitable for protection of compound 3. Both hydroxyl and imine groups were protected to give intermediate 4, which underwent fluorination and subsequent deprotection with 1 M HCl to give the final product ^{19}F-MAPP. Intermediate 4 was used as precursor for the subsequent radiolabeling optimization.

Radiochemistry.

Optimization for radiolabeling. The synthesis of ^{18}F-MAPP consists of 2 steps: radiolabeling and Boc deprotection (Fig. 1*B*). Starting from precursor 4, we first optimized the labeling step from solvents, bases, and temperature. The labeling was initially conducted with Krytofix 222 (K222)/K_2CO_3 as a phase transfer catalyst (PTC) in dimethyl sulfoxide at 90 °C for 10 min. These conditions resulted in multiple radioproducts, decomposition of the starting material, and, ultimately, low radiochemical yield of the desired product (23.5%). Further experiments were conducted with tetrabutylammonium bicarbonate (TBAB) as the PTC in MeCN at 60 °C, 70 °C, and 80 °C (*SI Appendix*, Table S1). We found that the TBAB and MeCN combination at 70 °C resulted in reasonable yields (56.6%) with minimal decomposition of the starting material. Following ^{18}F labeling, the Boc deprotection step was first conducted with 0.4 mmol aqueous HCl at 95 °C added directly to the labeling reaction mixture without any prior purification. The formation of ^{18}F-MAPP was monitored by radio–high-pressure liquid chromatography (HPLC) at 5, 15, and 30 min, showing the formation of the desired ^{18}F-labeled product quantitatively at 30 min (*SI Appendix*, Table S2, entries 1–3). The reaction rate increased by raising the HCl concentration but decomposition or defluorination was observed (*SI Appendix*, Table S2, entry 5). In the end, we identified 0.7 mmol HCl at 70 °C for 17 min as the appropriate Boc deprotection conditions for the following automated synthesis. The radio-HPLC chromatogram of the optimized labeling and deprotection steps before purification showed clean radiochemistry profiles (*SI Appendix*, Fig. S1*A*). *SI Appendix*, Fig. S1*B* demonstrates the radio-HPLC chromatogram of ^{18}F-MAPP before and after purification.

Automated synthesis of ^{18}F-MAPP. With the optimized radiolabeling and deprotection conditions, the synthesis of ^{18}F-MAPP was then moved into the automated synthesis module (*SI Appendix*, Fig. S2). The optimization results of automated synthesis of ^{18}F-MAPP (*SI Appendix*, Table S3) showed that the 2-step synthesis was completed in ∼80 min with a total radiochemical yield of 47% after decay correction. Subsequent syntheses were conducted with these conditions.

After automated synthesis followed by HPLC purification, the chemical purity of ^{18}F-MAPP was confirmed by the disappearance of the precursor 4 peak (t_R = 7.69 ± 0.059 min) and the formation of a new peak (t_R = 2.70 ± 0.074 min). The final product was collected according to the radiochromatogram and ultraviolet/visible (UV/Vis) chromatogram at 254 nm (*SI Appendix*, Fig. S1*C* and Table S4). The radiochemical identity of ^{18}F-MAPP was confirmed by coinjection with the reference compound ^{19}F-MAPP (*SI Appendix*, Fig. S1*D* and Table S4) and comparing the UV/Vis absorbance of ^{18}F-MAPP (*SI Appendix*, Fig. S1*E*) scaled to match that of ^{19}F-MAPP (*SI Appendix*, Fig. S1*F*). After HPLC purification, no free ^{18}F ions were detected (*SI Appendix*, Fig. S1*D*). The molar activity of ^{18}F-MAPP was 471.7 ± 146.7 mCi/μmol, computed using a standard curve relating UV absorption response to the mass of the nonradioactive ^{19}F-MAPP (*SI Appendix*, Fig. S1*G*). The final pH of ^{18}F-MAPP in an administering formulation (0.5% [wt/vol] sodium ascorbate in saline) was between 5 and 6. The log P of ^{18}F-MAPP was measured as ∼0.42 (*SI Appendix*, Table S5).

Stability of ^{18}F-MAPP. The ^{18}F-MAPP was stored in phosphate-buffered saline (PBS), and aliquots at different time points were injected to a radio-HPLC. As shown in Fig. 2*A*, a less polar peak formed over time, indicating gradual decomposition of ^{18}F-MAPP at room temperature. We hypothesized that the oxygen dissolved in PBS caused the degradation of ^{18}F-MAPP. Therefore, the radical scavenger, sodium ascorbate (0.5% wt/vol) in saline was used for formulation. Subsequently, ^{18}F-MAPP was stable for at least 4 h at room temperature in PBS (Fig. 2*B*). The plasma stability of the formulated ^{18}F-MAPP was also evaluated by incubating the radioprobe and mouse plasma at 37 °C. The peak integration of ^{18}F-MAPP in radio-HPLC confirmed the stability of ^{18}F-MAPP (>93%) over 4 h in plasma (Fig. 2*C*). Both PBS and plasma test solutions were exposed to air without removal of oxygen dissolved in the solutions.

Cytotoxicity. The 3-(4,5-dimethylthiazol-2-yl) 2,5-diphenyl-tetrazoilum bromide (MTT) assay with RAW 264.5 cells showed that there

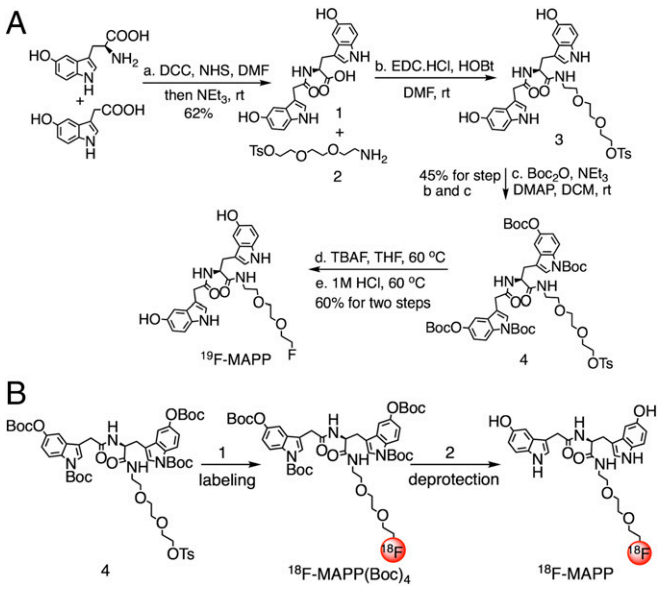

Fig. 1. Chemical synthesis. (*A*) Synthesis of nonradioactive ^{19}F-MAPP. DCM = dichloromethane; DMF = dimethylformamide; NEt3 = triethylamine; rt, room temperature; THF = tetrahydrofuran; NHS = *N*-hydroxysuccinimide; EDC.HCl = 1-ethyl-3-(3-dimethylaminopropyl)carbo-diimide; DMAP = 4-(dimethylamino)pyridine; TBAF = tetrabutylammonium fluoride. (*B*) Conditions of automated synthesis of ^{18}F-MAPP. (1) [^{18}F]-fluoride/TBAB, CH_3CN, 70 °C, 10 min; (2) HCl, CH_3CN, 70 °C, 17 min.

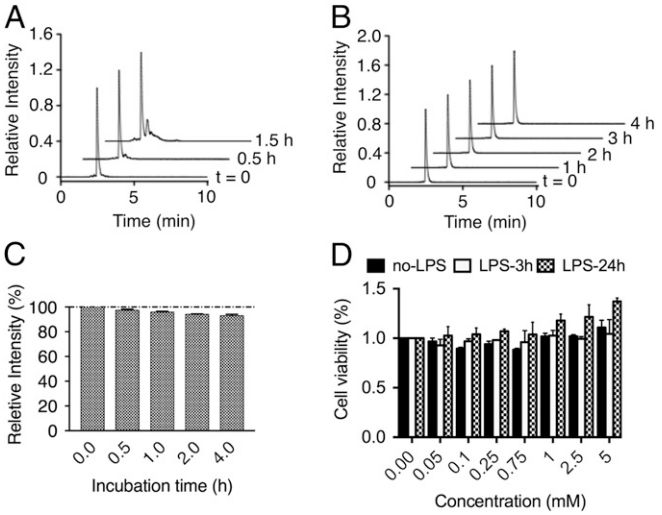

Fig. 2. Stability of ^{18}F-MAPP and its cytotoxicity. Relative intensity of ^{18}F-MAPP detected by a preparative radio-HPLC detector showed that (*A*) storage of ^{18}F-MAPP in PBS at room temperature degraded over time. (*B*) The ^{18}F-MAPP was stable up to 4 h at room temperature when stored in 0.5% Na ascorbate (wt/vol) in saline. (*C*) Stability of ^{18}F-MAPP incubated with plasma at 37 °C, 93% over 4 h ($n = 4$). (*D*) Cell toxicity of ^{19}F-MAPP incubated with RAW cells using the MTT assay. No cytotoxicity was observed from the radioprobe itself or after being activated by MPO. The raw cells were stimulated by LPS (3 and 24 h, respectively) to generate MPO ($n = 2 \times 3$ times of measurement for each).

was no significant cytotoxicity of ^{19}F-MAPP up to a concentration of 5 mM, which far exceeded the clinical dose (approximately nanomolar). Cells treated with lipopolysaccharide (LPS) stimulation to generate MPO (34) gave similar results, demonstrating that the activated products of ^{19}F-MAPP are also not toxic to the cells (Fig. 2*D*).

Protein binding by activated ^{18}F-MAPP. We incubated ^{18}F-MAPP with mouse plasma with or without MPO and glucose oxidase (GOX) for 60 min and then filtered it through a Biospin P-6 column to remove unbound radioprobe, followed by gel electrophoresis and autoradiography to determine if the activated radioprobe binds to proteins, which would allow the activated radioprobe to remain and accumulate at sites of activation. The less selective plant enzyme horseradish peroxidase (HRP) was used as a positive control. Strong signals were observed between 55 and 70 kDa which correspond to albumin when ^{18}F-MAPP was incubated with MPO or HRP (Fig. 3*A*, lanes 4 and 5). In contradistinction, there was only minimal signal when incubated without MPO and GOX, or with GOX only (Fig. 3*A*, lanes 1 and 2). No detectable signal was observed when no plasma was added because the unbound oligomers from the radioprobe after activation by MPO was filtered by the size exclusion column (Fig. 3*A*, lane 3).

Matrigel implantation animal experiment. We first evaluated ^{18}F-MAPP in vivo in Matrigel implantation animal experiments similar to those described in (34) to evaluate sensitivity to exogenous human MPO. The standardized uptake value (SUV) ratio on the MPO-containing side was 3- to 4.5-fold higher than that of the control side without MPO (Fig. 3 *B*, *1*) and 15- to 19-fold higher in contrast to muscle. To determine the sensitivity of ^{18}F-MAPP to MPO, different amounts of MPO (0, 15, 30 μL) were embedded in the gel. We observed a linear increase in the SUV in direct proportion to the amount of MPO embedded (Fig. 3 *B*, *2*). In a separate experiment to study the dynamic change of ^{18}F-MAPP in vivo, we found that ^{18}F-MAPP uptake in the MPO gel increased faster over time than that of the control gel without MPO (Fig. 4*A*), and the SUV ratio was 2.3- to 2.5-fold higher. This ratio was lower than that obtained from static imaging because the metabolism of the mice slowed down under the prolonged anesthesia during the dynamic imaging experiment, compared with the static imaging experiment in which the mice were allowed to resume normal activity after ^{18}F-MAPP injection until imaging.

Biodistribution. Biodistribution from dynamic imaging or necropsy at 3 h after ^{18}F-MAPP injection (Fig. 4 *B–D*) demonstrated that kidneys are the major organ to excrete ^{18}F-MAPP and had the highest uptake of ^{18}F-MAPP over 3 h, followed by liver and intestine. Of note, brain uptake was 3-fold higher compared with that of 3′-deoxy-3′-^{18}F-fluorothymidine (^{18}F-FLT), which does not cross an intact blood–brain barrier (BBB) (35), revealing that ^{18}F-MAPP can cross the BBB (Fig. 4*E*). We also evaluated the first pass uptake of ^{18}F-MAPP in different regions of the brain (*SI Appendix*, Fig. S3*A*). This showed that there was an initial increased uptake in the brain, especially in the frontoparietal lobes, followed by a decrease over the first 15 min. Subsequently, there was a slow increase over time in all regions of the brain (*SI Appendix*, Fig. S3*B*). The blood half-life of ^{18}F-MAPP was determined by counting the radioactivity of the blood samples. Using a 2-phase exponential decay model, we found the fast-phase half-life to be 0.26 min and the slow-phase half-life to be 4.66 min (Fig. 4*F*).

Paw CFA inflammation and treatment tracking. We next evaluated ^{18}F-MAPP in a mouse model of inflammation using complete Freund's adjuvant (CFA). CFA can induce acute inflammation (36) and generate MPO at the sites of inflammation (37, 38). This allows us to evaluate whether ^{18}F-MAPP is responsive to endogenously generated MPO. We injected CFA emulsion to induce inflammation in one forepaw of the mouse and used PBS on the other forepaw as control. The ^{18}F-MAPP uptake in the CFA-containing forepaw was 4 times higher than that in the PBS-injected forepaw, further demonstrating ^{18}F-MAPP's ability to report active inflammation (Fig. 5*A*).

To evaluate the specificity of ^{18}F-MAPP, we treated the CFA mice with either an MPO-specific irreversible inhibitor, PF-1355 (15, 23), or with vehicle. Uptake of ^{18}F-MAPP in the treated group decreased significantly compared with that of the control group as the result of the MPO activity inhibited by PF-1355 after accounting for the contralateral PBS-injected paw as control, using SUV ratios (SUVR) between the 2 sides (Fig. 5*B*). The mean inhibition was 57% (Fig. 5*C* and *SI Appendix*, Table S6), which matched previous ex vivo determination of PF-1355 inhibition on MPO activity of about 50% (15). The SUVs of the PBS-injected paws were low and similar to vehicle or PF-1355 treatment (*SI Appendix*, Fig. S4). These data revealed that ^{18}F-MAPP is specific and able to report MPO activity and can be used to monitor the treatment effect of MPO-targeted therapeutic drugs and to report the inflammatory response.

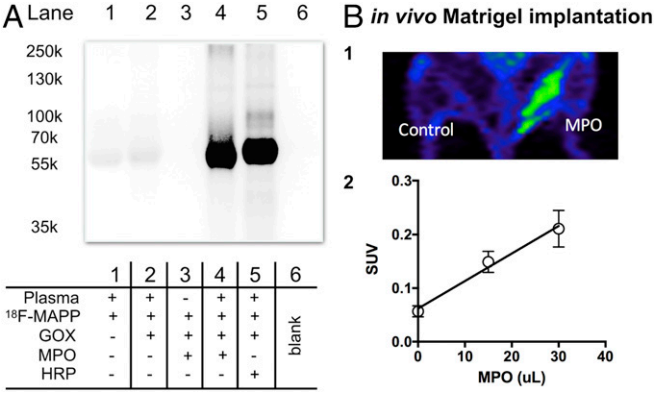

Fig. 3. Validation of ^{18}F-MAPP binding to proteins in vitro and in vivo. (*A*) Autoradiography demonstrates ^{18}F-MAPP binding to proteins in plasma after gel electrophoresis. Lane 4 with MPO and lane 5 with HRP showed strong signals compared with controls without MPO/HRP or plasma ($n = 3$). (*B*) PET imaging of Matrigel embedded with human MPO and GOX or GOX only as control (*B*, *1*). The uptake of ^{18}F-MAPP is linearly proportional to the amount of human MPO embedded in the Matrigel ($n = 3$ for each amount of MPO) (*B*, *2*).

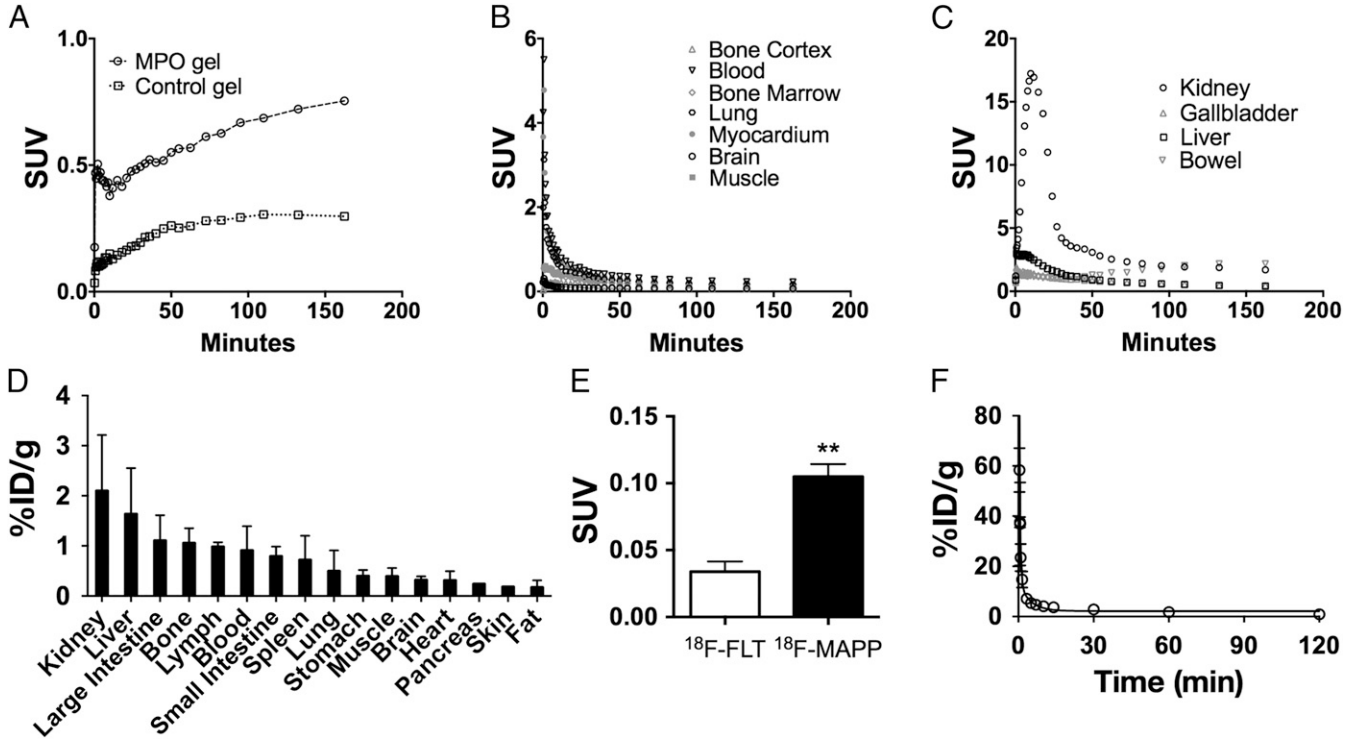

Fig. 4. Biodistribution of ^{18}F-MAPP. (*A*) Dynamic study of ^{18}F-MAPP uptake in MPO gel and control gel for 3 h. Signal in the MPO (15 μL) gel increased over time, while signal in the control gel remained low and decreased after 2 h. (*B* and *C*) The dynamic organ distribution and elimination of ^{18}F-MAPP over 3 h. Kidney is the major organ to excrete the radioprobe. (*D*) Biodistribution of ^{18}F-MAPP in the major organs of mice at 3 h after injection. Kidney, liver, and intestine have higher uptake of ^{18}F-MAPP compared with the other organs ($n = 3$). (*E*) SUV comparison between ^{18}F-FLT and ^{18}F-MAPP demonstrated that ^{18}F-MAPP can cross the blood–brain barrier ($P = 0.0095$), while ^{18}F-FLT does not cross the BBB ($n = 3$). (*F*) Blood half-life of ^{18}F-MAPP ($n = 2$). $^{**}P < 0.01$.

Myocardial infarction. As MPO is implicated in many cardiovascular diseases, we next evaluated ^{18}F-MAPP in a mouse model of myocardial infarction (MI). The ^{18}F-MAPP uptake in the infarct was markedly higher than that in the noninfarcted myocardium (Fig. 6*A*). Autoradiography of the ex vivo heart slices showed strong ^{18}F-MAPP uptake in the infarcted tissues compared with that of heart slices without infarction (Fig. 6*B*). In an MPO-deficient mouse with MI, no increased ^{18}F-MAPP uptake compared with wild-type myocardium without MI was observed (Fig. 6*C*), further demonstrating the specificity of ^{18}F-MAPP for MPO. In contrast, in the infarcted myocardium of wild-type mice, there was a more than 4-fold increased uptake compared with noninfarcted myocardium (Fig. 6*C*).

Discussion

Imaging inflammation is challenging because inflammation can cause both damage and repair. So far, no clinically available imaging agents can specifically differentiate either damaging or reparative inflammation. For example, phagocyte imaging with nanoparticles reports both damaging and reparative cells in myocardial infarction (39). Translocator protein imaging can detect active microglia and macrophages but does not inform whether these cells are actively damaging the tissue or participating in repair (40). Metabolic imaging with ^{18}F-fluorodeoxyglucose (FDG) similarly also reports both types of active inflammation and is limited in the brain and heart due to the high glucose avidity of these organs. On the other hand, MPO is a specific biomarker of damaging inflammation highly expressed by proinflammatory neutrophils and M1-type microglia and microphages but not by anti-inflammatory M2-type microglia and macrophages (9, 41, 42). Indeed, combining MPO-Gd imaging with nanoparticle phagocyte imaging allowed both damaging and reparative inflammation to be tracked over time (39). Until now, imaging MPO activity required the use of agents that have limited translational potential due to issues such as specificity, depth of penetration, low detection sensitivity, potential toxicity, and inability to cross the blood–brain barrier. Here we described ^{18}F-MAPP, which overcomes these limitations for reporting MPO activity in vivo. This radioprobe is highly specific and sensitive at very low doses, is nontoxic, and crosses the blood–brain barrier. We have optimized the synthesis and produced the radioprobe by

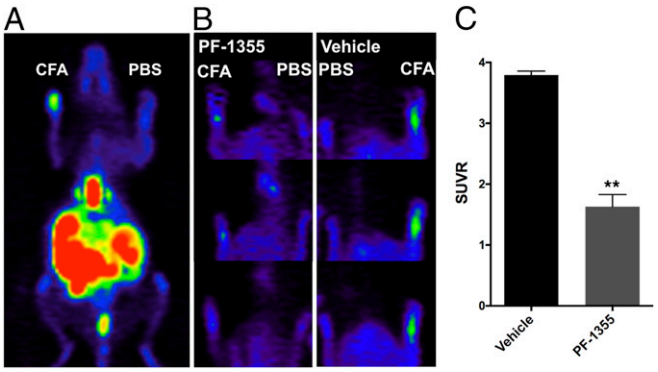

Fig. 5. Specificity and efficacy of ^{18}F-MAPP in CFA paw inflammation model. (*A*) The ^{18}F-MAPP uptake on the CFA-injected side was 4 times higher than that on the PBS-injected side. The CFA emulsion (CFA:PBS = 1:1) or PBS only was injected to the dorsal forepaws of the mouse, and ^{18}F-MAPP was administered after 24 h ($n = 3$). (*B*) Comparison of ^{18}F-MAPP uptake in mice treated with the specific MPO inhibitor PF-1355 to that of the vehicle-treated control mice. The treated and control mice were paired and imaged side by side 24 h after CFA injection. (*Left*) Mice treated with the MPO inhibitor PF-1355 (50 mg/kg) 1 h after CFA injection and every 6 h afterward. (*Right*) Mice treated with vehicle. (*C*) SUVR analysis (SUV ratio between CFA-injected and PBS-injected paws) showed that in the PF-1355-treated mice, MPO activity was inhibited by 57% ($n = 3$ per group). $^{**}P < 0.001$.

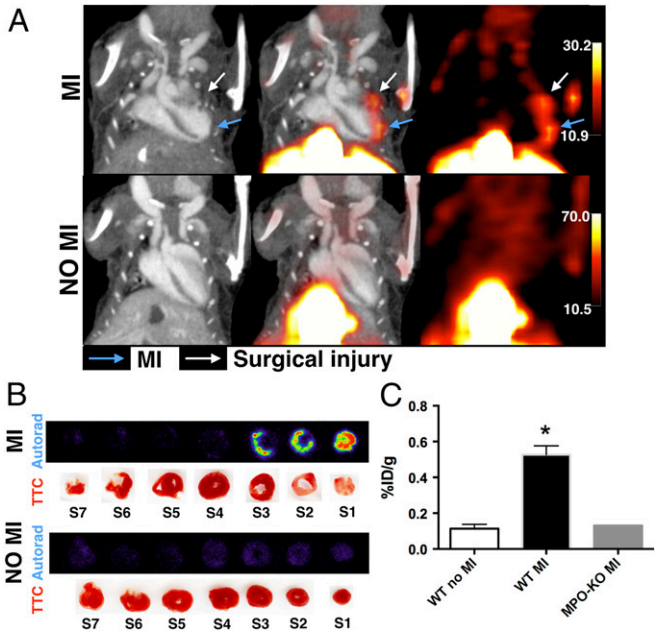

Fig. 6. The ^{18}F-MAPP PET imaging of MI. (*A*) The ^{18}F-MAPP uptake in wild-type mice with MI is much higher than that without MI. (*B*) Autoradiography of the heart slices with or without MI. The signals of heart slices 1, 2, and 3 with MI from autoradiography corresponded to that of the tetrazolium chloride (TTC) staining, while no detectable signal was observed from the heart slices without MI. (*C*) Comparison of the heart uptake of ^{18}F-MAPP between wild-type (WT) mice without MI, WT mice with MI, and a MPO-deficient (MPO-KO) mouse with MI ($n = 3$ for WT mice with or without MI, $n = 1$ for MPO-KO, $P = 0.029$ between WT with MI and without MI). $*P < 0.05$.

reproducible automated synthesis with satisfactory radiochemical yield, making it suitable for clinical translation in the near future.

The development of therapeutics targeting the inflammatory response and pathways demands potent noninvasive methods to detect the efficacy of these emerging drugs. Besides the aforementioned imaging methods to detect MPO activity, a ^{11}C-labeled MPO inhibitor, [^{11}C]AZD3241, that can enter monkey brains was reported for MPO imaging (43). However, the half-life of ^{11}C is short ($t_{1/2}$ = 20.4 min), and no selectivity and binding affinity of the agent have been revealed. Furthermore, inhibitor-based imaging agents might saturate the binding sites of the enzyme and interrupt its function and may not accurately report on enzyme activity, only its presence. Given the presence of endogenous MPO inhibitors, reporting merely on the presence of MPO may overestimate the location and degree of inflammation; ^{18}F-MAPP is a specific substrate, in which MPO oxidizes the 5-hydroxytryptophan moiety of ^{18}F-MAPP at the sites of inflammation (34). This causes free radicals to form and bind to proteins, causing local retention of the activated radioprobe (Fig. 3). Therefore, unlike inhibitor-based imaging agents, ^{18}F-MAPP does not interrupt the enzymatic function of MPO. Compared with the chelated MPO-Gd for MRI and its SPECT analogs, which provide a signal ratio between diseased and normal tissue of about 2-fold (29, 33), ^{18}F-MAPP has an improved sensitivity of 4-fold. Furthermore, because PET allows for quantification of the radioactivity and given that ^{18}F-MAPP's uptake is directly proportional to MPO activity (Fig. 3*B*), ^{18}F-MAPP can be used to quantify the degree of MPO activity in vivo. To accomplish this, a standard curve similar to Fig. 3 *B*, *2* may be generated and used to convert SUV to MPO. Because the image signal is dependent on the rate of delivery and oxidative retention by MPO, it is important to perform the in vivo experiments under the same timing conditions as those of the calibration experiment. In humans, the situation would be more complicated as individual variations in metabolism would affect the standard curve. Thus, quantitation in humans likely will require more complex modeling and will need additional data such as measuring blood levels of ^{18}F-MAPP radioactivity over time. Finally, ^{18}F-MAPP is able to accurately report on the degree of MPO inhibition when an irreversible MPO inhibitor is used to decrease inflammation in the paw inflammation model. Thus, this radioprobe would be a useful tool for drug development.

We found an increased brain uptake of ^{18}F-MAPP compared with ^{18}F-FLT (Fig. 4*E*), indicating that ^{18}F-MAPP can cross the blood–brain barrier. Evaluation of the uptake pattern in the brain (*SI Appendix*, Fig. S3) showed 2 phases of uptake in the brain. This pattern does not mirror that of blood uptake level, and thus, blood level does not explain the observation in the brain. The early phase of increased uptake is likely due to passive crossing of the blood–brain barrier, while the later increased uptake may be due to a transporter, such as an amino acid transporter, as MAPP contains moieties that resemble aromatic amino acids such as tryptophan. When combined with the increased sensitivity of PET imaging, this technology could open up new applications to image and study neurological diseases that have little to no blood–brain barrier breakdown, such as Alzheimer's disease and Parkinson's disease. Another potential application of ^{18}F-MAPP PET imaging is in cardiovascular diseases. In atherosclerosis, MPO is overexpressed by activated macrophages and macrophage-derived foam cells (44, 45) and is found in vulnerable plaques that may rupture (11). We and others have found that MPO imaging can identify highly inflamed plaques (46) and track treatment effects (47) in atherosclerotic plaques in rabbit and mouse models. We have also demonstrated the utility of ^{18}F-MAPP in MI imaging in this study. The increased sensitivity of ^{18}F-MAPP could enable the detection of damaging inflammation in many cardiovascular and neurological diseases at an earlier stage than currently possible. Such early detection would allow early treatment before irreversible damage occurs. Therefore, owing to the low dose needed for PET imaging and with its high sensitivity, specificity, stability, and favorable biodistribution and pharmacokinetics, ^{18}F-MAPP is a promising translational candidate to monitor MPO activity and damaging inflammation in patients.

Methods

Synthesis of Nonradioactive Compound ^{19}F-MAPP. The nonradioactive compound ^{19}F-MAPP was synthesized according to the synthetic route shown in Fig. 1*A*. The final step was purified by preparative HPLC to give the desired compound ^{19}F-MAPP. The important intermediates and final compound were characterized by ^{1}H NMR, ^{13}C NMR, and liquid chromatography–mass spectrometry. Additional details are given in *SI Appendix, SI Methods*.

Radiochemistry. The ^{18}F-MAPP was synthesized according to the synthetic route shown in Fig. 1*B*. Automated synthesis of ^{18}F-MAPP was carried out on the Synthra RNplus synthesizer (*SI Appendix*, Fig. S2). The automated synthesis took about 80 min, and the radiochemical yield of 47% was obtained after decay correction. Additional details are given in *SI Appendix, SI Methods*.

The ^{18}F-MAPP Characterization Experiments. We measured the lipophilicity of ^{18}F-MAPP by measuring the log P in a 1:1 mixture of 1-octanol and water. The specific activity was calculated using a standard curve relating ^{19}F-MAPP mass to UV absorption response. The pH of the final ^{18}F-MAPP in an administering formulation of PBS containing 0.5% (wt/vol) of sodium ascorbate was measured using pH indicator strips, demonstrating pH 5–6 from triplicates (*SI Appendix*, Fig. S5). Cytotoxicity of ^{19}F-MAPP was evaluated using RAW 264.7 cells with and without the presence of MPO using the MTT reduction assay. RAW 264.7 cells were treated with *Escherichia coli* LPS for 3 and 24 h, respectively, to generate MPO (34). Stability in plasma was measured by incubating ^{18}F-MAPP (~300 μCi) at 37 °C for 0 min, 30 min, 1 h, 2 h, and 4 h in mouse plasma. Protein binding of ^{18}F-MAPP was determined by incubating the radioprobe (~500 μCi) with bovine serum albumin (10 μL, 20 mg/mL), glucose (3 μL, 1g/mL), GOX (3 μL, 1 mg/mL), and MPO (5 μL, 2 mg/mL)/HRP (1 μL, 1 mg/mL) in PBS (total volume of 70 μL) at 37 °C for 60 min. Mixtures without MPO, MPO and GOX, or albumin were performed as control. The reaction mixture was filtered through Biospin P-6 columns (Bio-Rad) to remove unbound radioprobe,

followed by gel electrophoresis at 150 V for 50 min. Pharmacokinetics and biodistribution were determined after systemic injection of ^{18}F-MAPP via the tail vein of the C57BL/6J mice; blood samples were performed at different time points to determine clearance rate of ^{18}F-MAPP from the blood. The major organs of the mice were harvested after 3 h, and the radioactivity was assayed with a gamma counter (1480 Wizard 3, PerkinElmer). Additional details are given in *SI Appendix, SI Methods*.

PET-CT Imaging Experiments. This study was approved by and in compliance with Massachusetts General Hospital's Institutional Animal Care and Use Committee. Six- to ten-week-old female C57BL/6J mice (Jackson Laboratories) were used for all animal experiments. PET imaging was performed on a Siemens Inveon PET-CT scanner. The mouse was intravenously (i.v.) injected with 300–800 μCi of ^{18}F-MAPP under anesthesia (~2% isoflurane in oxygen).

Matrigel implantation experiment. Three hundred microliters of a 1:1 mixture of Matrigel and minimal essential medium containing a combination of GOX and/or MPO was injected subcutaneously (s.c.) into the ventral aspect of the thighs of the C57BL/6J mice. After 30 min, 300–600 μCi of ^{18}F-MAPP was injected i.v. in the bore of the PET scanner, and the mouse was imaged for 3 h for dynamic study or for 30 min 2 h postinjection.

Complete Freund's adjuvant inflammation and treatment tracking. C57BL/6J mice were injected s.c. with a 1:1 emulsion of CFA:PBS (40 μL of total volume) on the dorsal side of one forepaw under isoflurane anesthesia. PBS (40 μL) was injected on the other forepaw as control. In another experiment, mice were administered with PF-1355 (50 mg/kg) by oral gavage 1 h after the CFA injection with 3 more doses given every 6 h thereafter. The control group was treated with vehicle (10 mL/kg) in a similar fashion. After 24 h, 300–400 μCi of ^{18}F-MAPP were injected intravenously. Treated and untreated mice were paired and imaged side by side 2 h after radioprobe injection.

Myocardial infarction. MI was induced in C57BL/6J and MPO-deficient mice. Forty-eight hours after MI induction, 700–800 μCi of ^{18}F-MAPP were i.v. injected through the tail vein, and the mouse was imaged 3 h after administration. PET imaging of the heart was performed similar to what was described above. After PET imaging, the mice were killed, and organs were harvested for gamma well counting and autoradiography (heart only). Volumes of interest (VOI) were manually drawn for SUV quantification of the images in Inveon Research Workplace. For brain image analysis, VOIs were drawn within different regions of the brain while avoiding the ventricles and major blood vessels. Additional details are given in *SI Appendix, SI Methods*.

Statistical Analysis. Data are shown as mean ± SEM. P values < 0.05 were considered significant. Additional details are given in *SI Appendix, SI Methods*.

ACKNOWLEDGMENTS. This work was supported by grants from the NIH (R01 NS103998), the National Multiple Sclerosis Society, and Pfizer. C.W. was supported by a Research Scientist Award from the American Society of Neuroradiology. We thank Neil Vasdev and Timothy Shoup for their assistance with the initial radiochemistry experiments.

1. G. Chinetti-Gbaguidi, S. Colin, B. Staels, Macrophage subsets in atherosclerosis. *Nat. Rev. Cardiol.* **12**, 10–17 (2015).
2. N. G. Frangogiannis, The inflammatory response in myocardial injury, repair, and remodelling. *Nat. Rev. Cardiol.* **11**, 255–265 (2014).
3. A. Lampron, A. Elali, S. Rivest, Innate immunity in the CNS: Redefining the relationship between the CNS and its environment. *Neuron* **78**, 214–232 (2013).
4. A. N. Theofilopoulos *et al*., Sensors of the innate immune system: Their link to rheumatic diseases. *Nat. Rev. Rheumatol.* **6**, 146–156 (2010).
5. C. Reitz, T. Giuseppe, Inflammation, immune system and Alzheimer's disease: A review of the findings from the major GWAS studies. *J. Mol. Genet. Med.* **7**, 60 (2013).
6. S. Kathiresan, Myocardial Infarction Genetics Consortium, Genome-wide association of early-onset myocardial infarction with single nucleotide polymorphisms and copy number variants. *Nat. Genet.* **41**, 334–341 (2009). Correction in: *Nat. Genet.* **41**, 762 (2009).
7. C. Wu, F. Li, G. Niu, X. Chen, PET imaging of inflammation biomarkers. *Theranostics* **3**, 448–466 (2013).
8. D. A. Hammoud Molecular imaging of inflammation: Current status. *J. Nucl. Med.* **57**, 1161–1165 (2016).
9. F. K. Swirski *et al*., Myeloperoxidase-rich Ly-6C+ myeloid cells infiltrate allografts and contribute to an imaging signature of organ rejection in mice. *J. Clin. Invest.* **120**, 2627–2634 (2010).
10. S. J. Klebanoff, Myeloperoxidase: Friend and foe. *J. Leukoc. Biol.* **77**, 598–625 (2005).
11. B. S. van der Veen, M. P. de Winther, P. Heeringa, Myeloperoxidase: Molecular mechanisms of action and their relevance to human health and disease. *Antioxid. Redox Signal.* **11**, 2899–2937 (2009). Correction in: *Antioxid. Redox Signal.* **12**, 322 (2010).
12. S. J. Nicholls, S. L. Hazen, Myeloperoxidase and cardiovascular disease. *Arterioscler. Thromb. Vasc. Biol.* **25**, 1102–1111 (2005).
13. V. Rudolph *et al*., Myeloperoxidase acts as a profibrotic mediator of atrial fibrillation. *Nat. Med.* **16**, 470–474 (2010).
14. M. L. Brennan *et al*., Prognostic value of myeloperoxidase in patients with chest pain. *N. Engl. J. Med.* **349**, 1595–1604 (2003).
15. M. Ali *et al*., Myeloperoxidase inhibition improves ventricular function and remodeling after experimental myocardial infarction. *JACC Basic Transl. Sci.* **1**, 633–643 (2016).
16. S. Gellhaar, D. Sunnemark, H. Eriksson, L. Olson, D. Galter, Myeloperoxidase-immunoreactive cells are significantly increased in brain areas affected by neurodegeneration in Parkinson's and Alzheimer's disease. *Cell Tissue Res.* **369**, 445–454 (2017).
17. E. Gray, T. L. Thomas, S. Betmouni, N. Scolding, S. Love, Elevated myeloperoxidase activity in white matter in multiple sclerosis. *Neurosci. Lett.* **444**, 195–198 (2008).
18. E. Gray, T. L. Thomas, S. Betmouni, N. Scolding, S. Love, Elevated activity and microglial expression of myeloperoxidase in demyelinated cerebral cortex in multiple sclerosis. *Brain Pathol.* **18**, 86–95 (2008).
19. D. K. Choi *et al*., Ablation of the inflammatory enzyme myeloperoxidase mitigates features of Parkinson's disease in mice. *J. Neurosci.* **25**, 6594–6600 (2005).
20. R. J. Falk, J. C. Jennette, Anti-neutrophil cytoplasmic autoantibodies with specificity for myeloperoxidase in patients with systemic vasculitis and idiopathic necrotizing and crescentic glomerulonephritis. *N. Engl. J. Med.* **318**, 1651–1657 (1988).
21. R. B. Ruggeri *et al*., Discovery of 2-(6-(5-Chloro-2-methoxyphenyl)-4-oxo-2-thioxo-3,4-dihydropyrimidin-1(2H)-yl)acetamide (PF-06282999): A highly selective mechanism-based myeloperoxidase inhibitor for the treatment of cardiovascular diseases. *J. Med. Chem.* **58**, 8513–8528 (2015).
22. A. Jucaite *et al*., Effect of the myeloperoxidase inhibitor AZD3241 on microglia: A PET study in Parkinson's disease. *Brain* **138**, 2687–2700 (2015).
23. W. Zheng *et al*., PF-1355, a mechanism-based myeloperoxidase inhibitor, prevents immune complex vasculitis and anti-glomerular basement membrane glomerulonephritis. *J. Pharmacol. Exp. Ther.* **353**, 288–298 (2015).
24. S. Gross *et al*., Bioluminescence imaging of myeloperoxidase activity in vivo. *Nat. Med.* **15**, 455–461 (2009).
25. R. J. Goiffon, S. C. Martinez, D. Piwnica-Worms, A rapid bioluminescence assay for measuring myeloperoxidase activity in human plasma. *Nat. Commun.* **6**, 6271 (2015).
26. N. Zhang, K. P. Francis, A. Prakash, D. Ansaldi, Enhanced detection of myeloperoxidase activity in deep tissues through luminescent excitation of near-infrared nanoparticles. *Nat. Med.* **19**, 500–505 (2013).
27. P. Panizzi *et al*., Oxazine conjugated nanoparticle detects in vivo hypochlorous acid and peroxynitrite generation. *J. Am. Chem. Soc.* **131**, 15739–15744 (2009).
28. J. Shepherd *et al*., A fluorescent probe for the detection of myeloperoxidase activity in atherosclerosis-associated macrophages. *Chem. Biol.* **14**, 1221–1231 (2007).
29. J. W. Chen, M. Querol Sans, A. Bogdanov Jr, R. Weissleder, Imaging of myeloperoxidase in mice by using novel amplifiable paramagnetic substrates. *Radiology* **240**, 473–481 (2006).
30. J. Huang *et al*., Methods for measuring myeloperoxidase activity toward assessing inhibitor efficacy in living systems. *J. Leukoc. Biol.* **99**, 541–548 (2016).
31. H. Albadawi *et al*., Spinal cord inflammation: Molecular imaging after thoracic aortic ischemia reperfusion injury. *Radiology* **282**, 202–211 (2017).
32. Y. Zhang *et al*., Myeloperoxidase nuclear imaging for epileptogenesis. *Radiology* **278**, 822–830 (2016).
33. M. Querol Sans, J. W. Chen, R. Weissleder, A. A. Bogdanov Jr, Myeloperoxidase activity imaging using (67)Ga labeled substrate. *Mol. Imaging Biol.* **7**, 403–410 (2005).
34. E. Rodríguez, M. Nilges, R. Weissleder, J. W. Chen, Activatable magnetic resonance imaging agents for myeloperoxidase sensing: Mechanism of activation, stability, and toxicity. *J. Am. Chem. Soc.* **132**, 168–177 (2010).
35. W. Chen *et al*., Imaging proliferation in brain tumors with 18F-FLT PET: Comparison with 18F-FDG. *J. Nucl. Med.* **46**, 945–952 (2005).
36. J. C. Fehrenbacher, M. R. Vasko, D. B. Duarte, Models of inflammation: Carrageenan- or complete Freund's adjuvant (CFA)–induced edema and hypersensitivity in the rat. *Curr. Protoc. Pharmacol.* **56**, 5.4.1–5.4.4 (2012).
37. P. M. Chagas, B. da Cruz Weber Fulco, A. P. Pesarico, J. A. Roehrs, C. W. Nogueira, Effectiveness of bis(phenylimidazoselenazolyl) diselenide on a mouse model of inflammatory nociception. *Biomed. Pharmacother.* **96**, 56–63 (2017).
38. K. Okuda *et al*., New anthranilic acid derivative, EAntS-GS, attenuates Freund's complete adjuvant-induced acute pain in rats. *J. Surg. Res.* **175**, 265–270 (2012).
39. E. J. Keliher *et al*., Polyglucose nanoparticles with renal elimination and macrophage avidity facilitate PET imaging in ischaemic heart disease. *Nat. Commun.* **8**, 14064 (2017).
40. M. K. Chen, T. R. Guilarte, Translocator protein 18 kDa (TSPO): Molecular sensor of brain injury and repair. *Pharmacol. Ther.* **118**, 1–17 (2008).
41. P. P. Bradley, R. D. Christensen, G. Rothstein, Cellular and extracellular myeloperoxidase in pyogenic inflammation. *Blood* **60**, 618–622 (1982).
42. W. Scholz *et al*., Initial human myeloid/dendritic cell progenitors identified by absence of myeloperoxidase protein expression. *Exp. Hematol.* **32**, 270–276 (2004).
43. P. Johnström *et al*., Development of rapid multistep carbon-11 radiosynthesis of the myeloperoxidase inhibitor AZD3241 to assess brain exposure by PET microdosing. *Nucl. Med. Biol.* **42**, 555–560 (2015).
44. S. Sugiyama *et al*., Macrophage myeloperoxidase regulation by granulocyte macrophage colony-stimulating factor in human atherosclerosis and implications in acute coronary syndromes. *Am. J. Pathol.* **158**, 879–891 (2001).
45. P. Libby, Inflammation in atherosclerosis. *Nature* **420**, 868–874 (2002).
46. J. A. Ronald *et al*., Enzyme-sensitive magnetic resonance imaging targeting myeloperoxidase identifies active inflammation in experimental rabbit atherosclerotic plaques. *Circulation* **120**, 592–599 (2009).
47. I. Rashid *et al*., Myeloperoxidase is a potential molecular imaging and therapeutic target for the identification and stabilization of high-risk atherosclerotic plaque. *Eur. Heart J.* **39**, 3301–3310 (2018).